ADVANCED FUNCTIONAL MATERIALS
www.afm-journal.de

A Fabrication Strategy for Reconfigurable Millimeter-Scale Metamaterials

*Hayley D. McClintock, Neel Doshi, Agustin Iniguez-Rabago, James C. Weaver, Noah T. Jafferis, Kaushik Jayaram, Robert J. Wood, and Johannes T. B. Overvelde**

Rather than depending on material composition to primarily dictate performance metrics, metamaterials can leverage geometry to achieve specific properties of interest. For example, reconfigurable metamaterials have enabled programmable shape transformations, tunable mechanical properties, and energy absorption. While several methods exist to fabricate such structures, they often place severe restrictions on manufacturing materials, or require significant manual assembly. Moreover, these arrays are typically composed of unit cells that are either macro-scale or micro-scale in dimension. Here, the fabrication gap is bridged, and laminate manufacturing is used to develop a method for designing reconfigurable metamaterials at the millimeter-scale, that is compatible with a wide range of materials, and that requires minimal manual assembly. In addition to showing the versatility of this fabrication method, how the use of laminate manufacturing affects the behavior of these multi-component arrays is also characterized. To this end, a numerical model that captures the deformations exhibited by the structures is developed, and an analytic model that predicts the strain of the structure under compressive stress is built. Overall, this approach can be leveraged to develop millimeter-scale metamaterials for applications that require reconfigurable materials, such as in the design of tunable acoustics, photonic waveguides, and electromagnetic devices.

1. Introduction

In addition to intrinsic properties based on the chemical composition of their components, metamaterials derive their material properties from their often elaborate physical structures. These complex geometric forms can be designed to enable mechanical properties thought to be unrealizable in amorphous or crystalline materials, such as negative compressibility,[1,2] negative thermal expansion,[2,3] vanishing shear modulus,[4,5] and negative Poisson's ratio.[6,7] In addition to employing structure to directly affect mechanical performance, recent years have seen the development of multifunctional metamaterials, in which the behavior of the material is dictated through geometrical reconfigurations of their internal structure. These designs allow for variable geometric states, each with the capacity to exhibit unique properties by altering the orientation of the unit cells, with applications ranging from microwave absorbers,[8,9] to acoustics,[10,11] and optics.[12,13]

To design reconfigurable metamaterials, researchers often take inspiration from origami principles, describing the material's structure with a set of periodic linkages. The stiffness of these structures is typically highly anisotropic, where low stiffness represents an internal folding mode along which the structure of the metamaterial can be reconfigured, and the high stiffness directions can be employed

H. D. McClintock
Fu Foundation School of Engineering and Applied Science
Columbia University
New York, NY 10027, USA

N. Doshi
Intelligence Community Postdoctoral Research Fellowship Program
Massachusetts Institute of Technology
Cambridge, MA 02139, USA

A. Iniguez-Rabago, J. T. B. Overvelde
Designer Matter Department
AMOLF
Science Park 104, Amsterdam 1098XG, the Netherlands
E-mail: overvelde@amolf.nl

The ORCID identification number(s) for the author(s) of this article can be found under https://doi.org/10.1002/adfm.202103428.

DOI: 10.1002/adfm.202103428

J. C. Weaver, N. T. Jafferis, R. J. Wood
John A. Paulson School of Engineering and Applied Sciences
Harvard University
Cambridge, MA 02138, USA

N. T. Jafferis
Department of Electrical and Computer Engineering
University of Massachusetts Lowell
Lowell, MA 01854, USA

K. Jayaram
Paul M. Rady Department of Mechanical Engineering
University of Colorado Boulder
Boulder, CO 80309, USA

J. T. B. Overvelde
Institute for Complex Molecular Systems and Department of Mechanical Engineering
Eindhoven University of Technology
P.O. Box 513, Eindhoven 5600MB, the Netherlands

Table 1. Metamaterials fabricated using different methods and materials, spanning from the macro-scale to the micro-scale.

	Characteristic length	Metamaterial	Fabrication method	Constituent material
[27]	100–200 mm	Prismatic architected material	Laser cutting	Cardboard with double-sided tape
[24]	50–100 mm	2D orthotropic lattice structure	3D printing	Vero white plus
[28]	30–100 mm	Shape reconfigurable material	Laser cutting	Polytetrafluoroethylen sheets
[17]	≈60 mm	Extruded cube tessellation	Laser cutting	Polyethylene terephthalate with double-sided tape
[6]	30–40 mm	Bucklicrystals	Casting	Soft silicon-based rubber (vinyl polysiloxane)
[29]	≈30 mm	Programmable origami matter	Laser cutting	E-glass fiber (104 weave), impregnated with RS-30 resin and two component silicone
[25]	≈20 mm	Biholar sheet	Casting	Two component silicone elastomer
[26]	≈20 mm	Periodic monodisperse circular hole arrangements	Casting	Two component silicone elastomer
[23]	12.5 mm	Interleaved tube cellular structure	3D printing	UV photocured acrylic
[36]	10 mm	Stent graphs	PμSL	Ni-rich TiNi SMA foils
[30]	8 mm	Hierarchical kirigami	Laser cutting	Polyester elastic sheet
This work	8 mm	Sarrus linkage metamaterial	Laminate fabrication	FR4 sheets and polyimide films
[16]	6 mm	Miura-ori sheet	DLP 3D printing	Photocurable resin
[35]	100–500 µm	Hollow-tube nanolattice with an octet-truss geometry	SPPW	Nickel-phosphorous
[15]	25 µm	Miura-ori tubes assembly	TPL	Two-photon liquid photoresist
[34]	15 µm	Hexagonal frames with integrated horizontal test struts	DLW	Two-photon liquid photoresist covered with alumina
[32]	10 µm	3D composite microarchitectures	TPL	Alumina
[33]	10 µm	Bow-tie metamaterial	DLW	Two-photon liquid photoresist
[31]	5–15 µm	Hollow-tube nanolattice with an octet-truss geometry	TPL	Alumina

to bear applied loads. Importantly, the use of folding places significant constraints on the internal architecture and materials used, as a result of stress and deformation that localizes at folds. For example, achieving such deformation requires either the use of large differences in material thickness, the use of materials with different elastic moduli, or both.

While many origami-inspired reconfigurable metamaterials exist, including those based on the Miura-ori pattern,[14–16] cubic lattices,[17] the hypar,[18] the Sarrus linkage,[19,20] and other origami patterns,[21,22] most of them are not yet available at the desired application-specific length-scales or cannot be fabricated using a wide range of materials. For comparison purposes, an overview of different metamaterial geometries, their fabrication methods, constituent materials, and characteristic length scales are shown in **Table 1**. While a variety of manufacturing techniques such as 3D printing,[23,24] casting,[6,25,26] and laser cutting[17,27–30] can be used to produce these foldable metamaterials at the macro-scale (unit cells >1 cm), most of these techniques require manual assembly of the metamaterial's sub-components, a task that grows in complexity, and quickly becomes intractable, as the number of components increases. In contrast, more automated and highly parallel fabrication techniques such as two photon lithography (TPL),[15,31,32] direct-laser-writing (DLW) lithography,[33,34] self-propagating polymer waveguides (SPPW),[35] and projection micro-stereolithography (PμSL)[36] can be used to manufacture metamaterials at the micron- and sub-micron-scale (unit cells less than 1 mm). While manual assembly can be completely circumvented at this scale, other disadvantages emerge. For example, these techniques use a very limited diversity of materials for fabrication, and since they rely on the photo-polymerization of cross-linkable resins from the bulk, do not permit the production of multi-material constructs.

To overcome these limitations and bridge the gap between macro- and micro-scale metamaterials (i.e., to develop millimeter-scale metamaterials) the development of new fabrication strategies is required. If realized, these millimeter-scale reconfigurable metamaterials could be used in the design of medical devices,[22] end-effectors,[37] and functional structures (e.g., handles, wrenches, and pliers[38]). To address these needs, we employ laminate fabrication techniques, typically used for the production of printed-circuit microelectromechanical systems (PC-MEMS)[39] and smart composite micro-structures (SCM).[29,40] Previously, these techniques have been successfully employed to design and manufacture complex, articulated 3D mechanisms,[41–43] and as such, have several key advantages for the design of reconfigurable metamaterials. For example, the resulting mechanisms start from, and can be folded back into, a flat configuration. Moreover, the fabrication of these structures requires minimal manual assembly, and in certain cases, the assembly process can be completely automated for improved alignment and precision.[43] The laminate manufacturing process also accepts a wide range of materials, including fiberglass, carbon fiber, and various metals and polymers, since the only constraints are the temperature and pressure applied during bonding.[40] Finally, using a lamination-based manufacturing process also offers additional advantages such as scalability. For example, dimensional parameters can easily be adjusted for micro- to macro-scale applications.[44]

In the present study, we use a four-sided Sarrus linkage (**Figure 1**) as the unit-cell for our metamaterial, as its simple single degree of freedom (DOF) kinematics and layered structure make it well-suited for fabrication using laminate manufacturing approaches.[43] It is important to note, however, that a variety of

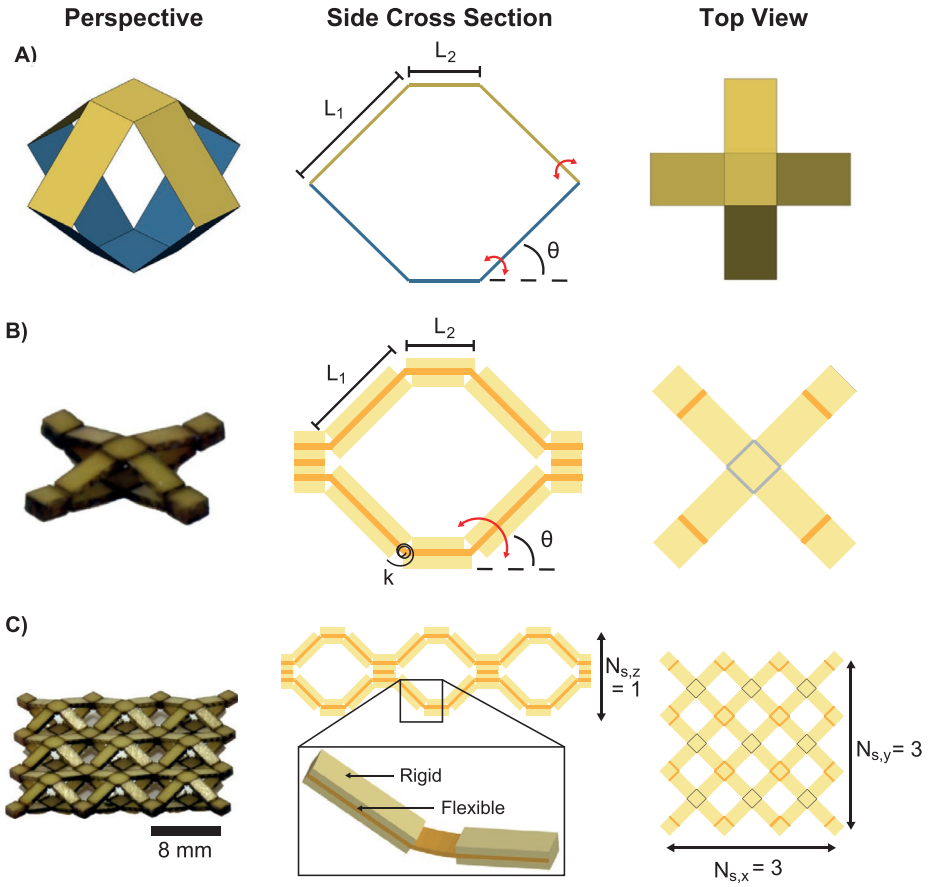

Figure 1. Sarrus linkage array design. A) An ideal four-sided Sarrus linkage. B) A single fabricated Sarrus linkage unit cell. In this context, we define a unit cell as a four-sided Sarrus linkage with arm lengths of L_1 and L_2, which consists of 16 hinges with stiffness k, with each hinge able to rotate by amount θ. In our fabrication approach, an extra layer of polyimide remains where the top and bottom laminates connect as a remnant from the spacing layer that prevents the arms from sticking together. C) A fabricated 3×3 Sarrus linkage array, where a single layer in the array is produced by diagonally connecting an arbitrary number of unit cells. We defined $N_{s,x}$, $N_{s,y}$, $N_{s,z}$ as the number of unit cells along the width, length, and depth of the array, respectively.

different unit-cells can be used, including other one-DOF linkages (e.g., an *n*-sided Sarrus, a scissor linkage, a four-bar, etc.), as well as more complex multi-DOF linkages (e.g., a spherical five- or six-bar or even a delta robot[45]). Here, a four-sided Sarrus linkage allows us to focus on the core contributions of our work: 1) developing a method for fabricating a large number of moving components with minimal manual assembly from a variety of manufacturing materials, and 2) characterizing the behavior of laminate metamaterials, with comparison to the kinematics of the ideal linkage-based system.

To facilitate fabrication using laminate manufacturing, the Sarrus linkage design was modified to use flexure hinges instead of pin joints. Consequently, we explore whether the flexure-based mechanism impacts the metamaterial's behavior and find experimentally that two modes occur in the array: a compression mode that is explained by the ideal behavior of the Sarrus linkage and a bending mode that is only possible when considering additional hinge deformation. Simulations are also performed to explore the deformations induced by these two modes, taking into consideration off-axis hinge deformations (i.e., shear and torsion). Based on these simulations, we focus on empirically characterizing the compression mode in greater detail since the bending mode resulted in only local deformations. From these studies, we find that hinge geometry can be used to alter the effective modulus of the metamaterial, while keeping the deformation of the compression mode the same. We then build Hookean and viscoelastic models of the hinge's bending behavior, and use these models to predict the stress–strain response of the metamaterial along the compression mode. Our results show that the Hookean model provides a good approximation for the stress–strain response of the physical metamaterial for this mode. From these simulations and experimental studies, we demonstrate that this millimeter-scale fabrication method can be used to create materials exhibiting specific deformation modes and effective moduli. As such, these efforts help lay the groundwork for developing a wide variety of new reconfigurable metamaterials for applications such as electromagnetic devices,[46,47] wave guides,[48] or deployable structures[49] that exploit the reconfigurability of these materials.

2. Results

2.1. Metamaterial Design and Fabrication

To understand the array's behavior, we begin by introducing the ideal kinematics of the reconfigurable metamaterial that is used

here as a case study. The design of the array is based on a relatively simple linear mechanism, known as a four-sided Sarrus linkage (henceforth Sarrus linkage), shown in Figure 1A. Sarrus linkages convert a limited circular motion to a linear motion using two parallel horizontal plates connected by hinged rectangular plates (Figure 1A). This mechanism is ideally composed of 12 one-DOF hinges (i.e., pin joints, connecting several rigid faces), the deformation of which is a consequence of the articulation of the hinges (here we assume that the rigid plates do not deform). With this description, the motion of this linkage can be fully characterized by a single configuration variable, θ. The height h and the width w of the linkage are given by

$$h = 2L_1 \sin(\theta), \quad w = 2L_1 \cos(\theta) + L_2 \tag{1}$$

in which L_1 is the length of the hinged rectangular plate, L_2 is the length of the square horizontal plate, and $0 \leq \theta \leq \pi/2$ is the range of the single DOF. Aligning several Sarrus linkages diagonally in a cubic lattice forms a metamaterial that extends each linkage's behavior while still maintaining a single DOF θ (Figure 1). For the physical Sarrus linkage array, we constructed unit cells that consist of 16 hinges with individual arm lengths, L_1, ranging from 1 to 3 mm (Figure 1B). The physical array has 16 hinges as opposed to the 12 in the ideal linkage since the joint that connects the top platform to the bottom platform is split into two hinges. This splitting, however, does not affect the general behavior of the linkage, and therefore, is not explicitly modeled in future sections. This configuration enables the linkage to be fabricated using laminate manufacturing, as the entire design can fold flat. An array consists of diagonally tiled unit cells (Figure 1C), in which two opposite plates change their separation distance. Each plate is made from two stiff outer layers with a flexible polyimide layer in the middle bonded by a thin thermoplastic adhesive sheet.[50] To create hinges, the stiff layers are selectively cut prior to bonding to reveal the polyimide at the required location. The two plates are then bonded together to create the Sarrus linkage (**Figure 2**A). Note that an additional layer of polyimide is added between the top and bottom plates. This extra layer acts as a removable spacer between the arms of the top and bottom plates to prevent them from sticking together and inhibiting deployment. After a final release cut, the structure is manually unfolded and the spacers are removed. This fabrication method yields a metamaterial with multiple hinges and requires minimal manual assembly.

The flexibility of this fabrication approach allows for a variety of different array designs, as shown in Figure 2B–G. For example, different array sizes can be achieved by varying the number of connected unit cells, that is, varying $N_{s,x}$ or $N_{s,y}$, (Figure 2B) or the array dimensions (Figure 2C). To create multi-layer arrays, that is, $N_{s,z} > 1$, multiple Sarrus arrays can be bonded on top of each other (Figure 2D–F). Theoretically, any number of arrays could be stacked together. Here, a maximum of three layers were used, as the laser micromachining system employed in the present study has a limit to the thicknesses of the alignment frames it can successfully cut. However, this limitation can be overcome if each layer is fabricated independently and then aligned and bonded to eliminate the final release cut step. Different structure designs can also be achieved by connecting unit cells of different sizes, or by selectively layering unit cells (Figure 2F). Finally, the materials for both the rigid and flexible layers can be varied. In Figure 2G, for example, we show that arrays can also be made with steel or carbon fiber. The thickness of the rigid or flexible layers can also be varied. Here, we used 7.5 mm, 12.5 µm, and 25 mm polyimide as the flexible layer.

While laminate manufacturing provides several benefits when manufacturing a millimeter-scale metamaterial, it is also important to consider the effect of manufacturing limitations that cause our physical Sarrus linkage to deviate from its ideal design. For example, when using the laminate manufacturing process, rigid faces and pin joints are approximated by composite laminates and hinges, respectively.[40] Consequently, it is important to verify that the deformation of these structures is localized to the hinges, and that the hinges faithfully approximate single DOF pin joints.

To localize the deformation of our structures to the hinges, we ensure that the bending stiffness of the hinges was much lower than the bending stiffness of the faces. This can be achieved by designing the faces to be much thicker than the hinges ($T_f \gg T_h$) or by choosing the Young's modulus of the face material to be significantly higher than that of the hinge material ($E_f \gg E_h$). Here we do both. We use 250 to 300 µm thick FR4 sheets for the rigid faces and 7.5 to 25 µm thick polymide (Dupont, Kapton) for the hinges. We selected FR4 and polymide as they are widely available low-cost materials. We also measured the face material's modulus as 21.74 GPa (Note S1, Supporting Information) via a three-point bending test (Figure S1, Supporting Information), and confirmed the reported modulus of the hinge material to be 2.71 GPa.[51] It should be noted that the face material's modulus is dominated by that of the rigid layer and is within the reported range for FR4.[52] These considerations, namely that $T_f > 10T_h$ and $E_f \approx 8E_h$, in principle ensures that the deformation of the structure will be localized to the hinges.

Second, we need to ensure that the hinges behave in accordance with the pseudo-rigid body model.[44] Following the guidelines for fabricating small-length flexural pivots,[44] we designed the faces to be much longer than the hinges: face lengths L_1 and L_2 range from 1 to 3 mm, while hinge lengths, W_h, were 0.2 mm. This design ensures that hinge-bending is well-approximated by the motion of an-ideal pin-joint (i.e., rotation about a fixed axis). Moreover, we ensure that the hinges are long enough to rotate without the faces colliding, which depends on the thickness of the laminate, T_f. Here we size the hinges to support a rotation of $\theta_{\max} = 75°$, that is $W_h \geq \frac{\theta_{\max}}{2T_f}$, which provides a good compromise between maximizing the travel and maintaining the small-length flexural pivot assumption. However, it is difficult to eliminate DOFs introduced by off-axis deformations of the hinges (i.e., torsion and shear). To fully understand the impact of these additional DOFs, we fabricated a linkage array consisting of $5 \times 5 \times 3$ unit cells, as shown in **Figure 3**A. Consistent with the ideal behavior, this metamaterial can be deformed along the predicted mode in which all the hinges deform equally (Figure 3B). However, we also observe an additional deformation mode, a bending mode (Video S1, Supporting Information), that is not consistent with the assumption that all hinges are one DOF (Figure 3C).

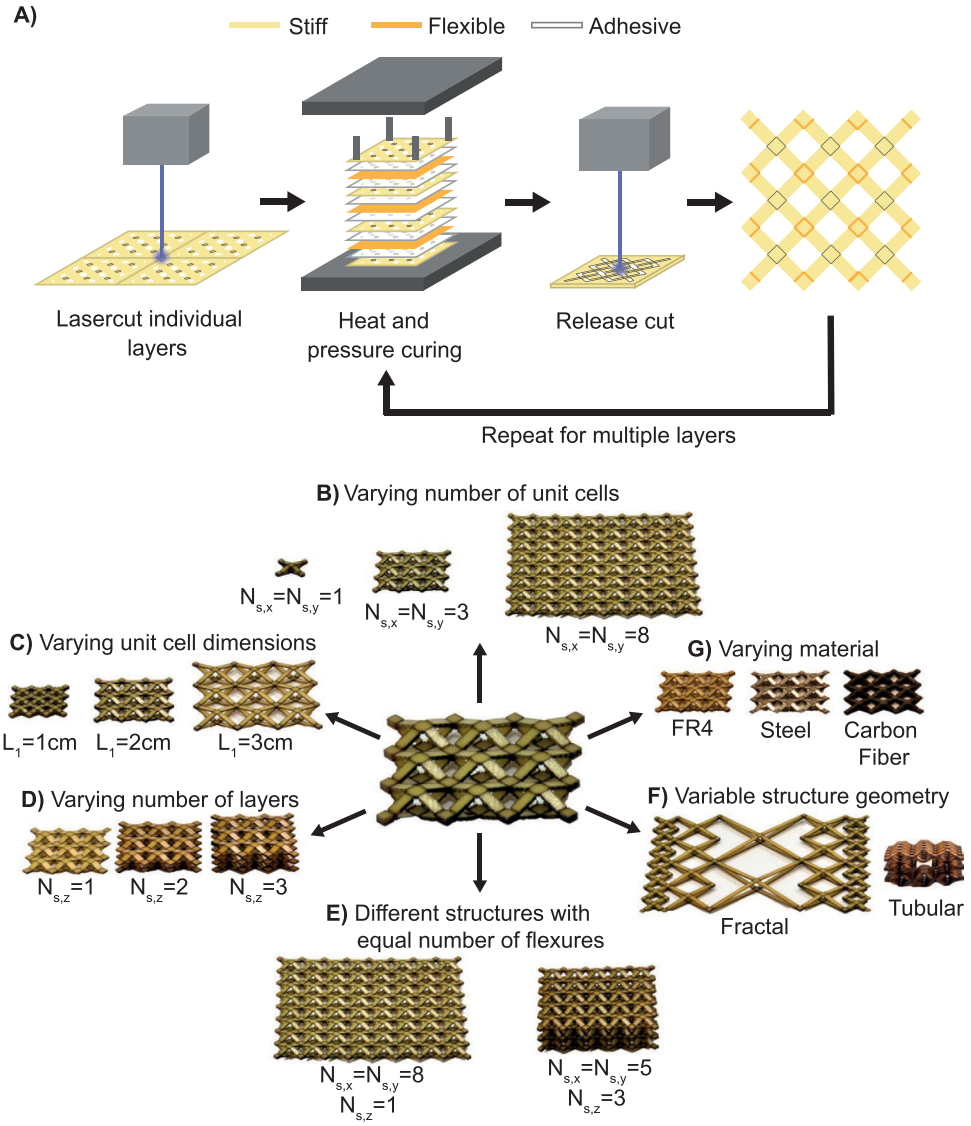

Figure 2. Metamaterial array manufacturing. A) Arrays are manufactured using laminate fabrication techniques. Individual layers are first laser-cut, then stacked and aligned with heat and pressure applied. Once cured, the entire laminate is laser-cut again to release the structure. Either single-layer or multi-layer arrays can be fabricated. For a multi-layered array, single-layer arrays are first fabricated with a remaining alignment frame, and then stacked and aligned. Once cured, the laminate is cut again with a final release cut. B) Single layer arrays with a single unit cell, an array with $N_{s,x} = N_{s,y} = 3$, and an array with $N_{s,x} = N_{s,y} = 8$ unit cells. C) Varying array dimensions using the same number of unit cells and altering the unit cell dimensions. D) Demonstration of how arrays can be layered. Arrays with $N_{s,z}$=1 layer, $N_{s,z}$=2 layers, and $N_{s,z}$=3 layers are shown. E) An example of different shaped structures that both have ≈1000 hinges. F) Examples of different structural geometries that can be created using the base unit cell and variations of the base unit cell. G) Demonstration of array fabrication with FR4, steel, and CF stiff layers.

2.2. Numerical Model of Folding Behavior

To understand these deformation modes in more detail, we implement a numerical model. Since the stiffness of the hinge is much smaller than the bending stiffness of the laminate, we can model the Sarrus linkage array as an origami-like structure.[53] This origami structure is approximated by zero thickness faces (laminates) connected through hinges (polyamide) as seen in Figure 3D. While the hinges can fold and are modeled as torsional springs, we use a zero stiffness hinge in the model to easily determine if a folding mode is purely rigid or requires deformation of the faces. The hinges can also have additional deformations, such as shearing or twisting as they are actually small-length flexural pivots. We account for these deformations by incorporating them as deformation of the faces. For this approach, the faces are allowed to stretch but not bend,[53] and their stiffness is approximated by linear springs located at the edges and diagonals (Figure 3D). The addition of these DOFs makes the motion of each unit cell partially independent from that of its neighbors. Note that this elastic model was chosen due to its computational convenience and despite the fact that it does not accurately represent real deformation, it qualitatively describes the real behavior of the structure using the condition of small face deformations.

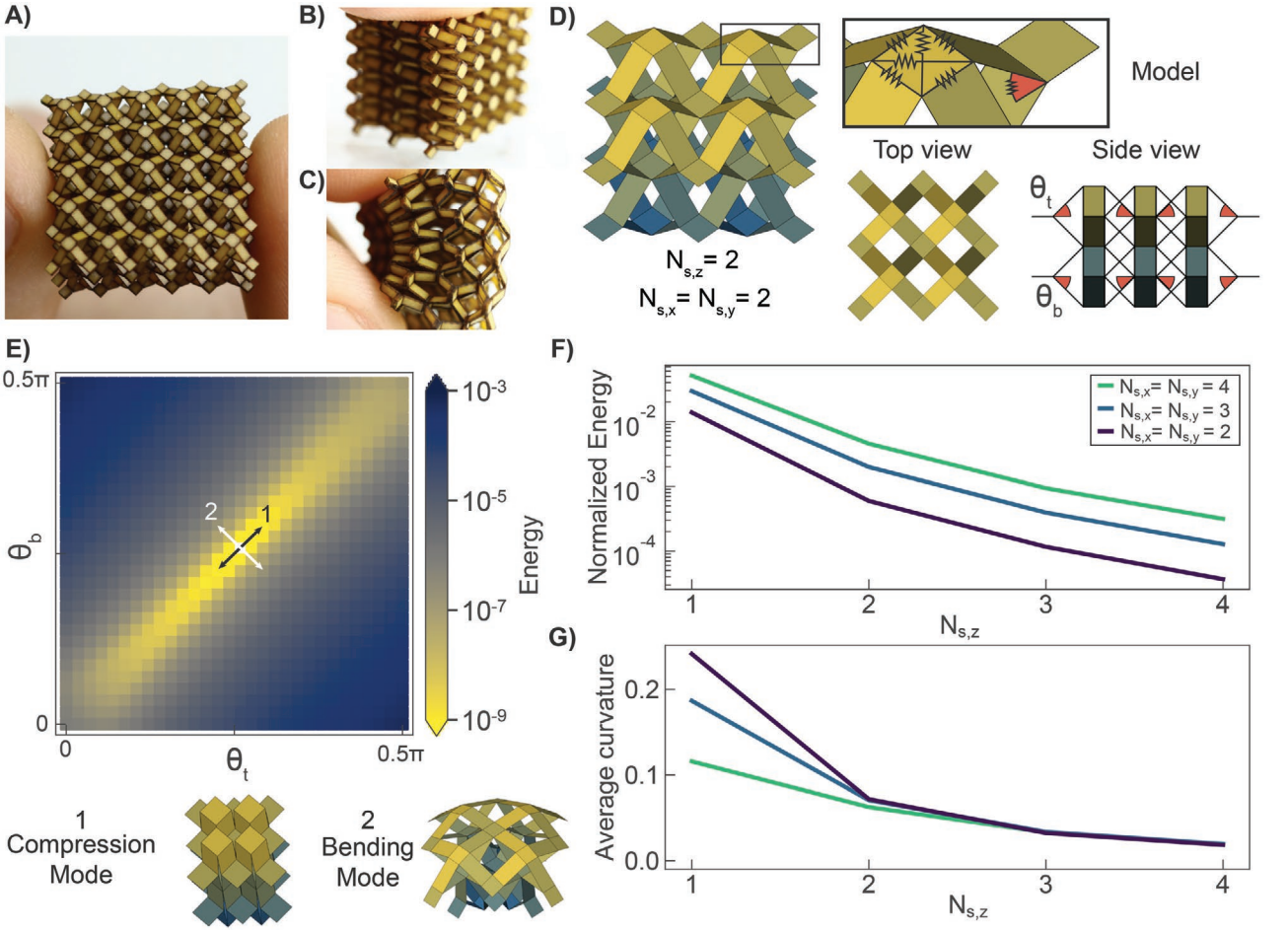

Figure 3. Analysis of the Sarrus linkage-based metamaterial. A) A fabricated array with $N_{s,x} = 5$, $N_{s,y} = 5$, and $N_{s,z} = 3$. Deformation of this array along the B) compression and C) bending modes. D) A model of the same metamaterial with $N_{s,x} = 2$, $N_{s,y} = 2$, and $N_{s,z} = 2$. We show the angles that are actuated in the simulation, θ_t and θ_b, in order to model the movement of the two modes. E) The elastic energy of this array when assigning specific angles to θ_t and θ_b. F) The energy and G) the curvature of the structure at the extremes of the bending modes for arrays with varying unit cells and layers.

To obtain the deformation of the structure, we use an optimization analysis based on its elastic energy.[53] We deform the structure by applying a local actuation to a selection of the hinges. This actuation corresponded to folding these hinges to specific angles as if experimentally performing a rotation controlled test, and is modeled as an additional rotational spring at these hinges. These additional springs form an energy penalty that is added to the elastic energy of the structure to obtain a total energy. By minimizing the total energy, we ensure that the structure deformed according to the applied local actuation. Since the stretching of the faces, corresponding to the shearing or twisting of the hinges, has a much higher stiffness than the bending of the hinges, which is zero in our model, the minimum energy configuration minimizes face deformation for the angles specified by the local actuation, mimicking the deformations in the experiments.

Following this approach, we are able to find the same two modes that are observed experimentally (Video S2, Supporting Information). To reproduce both deformation modes (Figure 3B,C) we actuate all of the hinges on the top and bottom layer, θ_t and θ_b, respectively (Figure 3D). These angles represent the DOFs for each unit cell and thus can vary from 0 to $\pi/2$. We obtain the normalized elastic energy for a structure with $N_{s,x} = N_{s,y} = N_{s,z} = 2$ (Figure 3E) in this angle range. As expected, the energy along the compression mode $(\theta_t = \theta_b)$ does not increase and remains at zero. This observation implies that all of the deformation is localized to the hinges and no stretching of the faces occurs. In other words, the compression mode is rigidly foldable. In contrast, the bending mode $(\theta_t + \theta_b = \pi/2)$ requires an increase in energy that originates from stretching the faces of the structure, such that this mode is not rigidly foldable. It is important to note that for the physical prototype, this bending mode is likely the result of additional deformations of the hinges, for example, shearing or twisting, as we verified that it is unlikely for the laminates to stretch.

To explore this behavior, we vary both the number of layers, $N_{s,x}$ and $N_{s,y}$, and the number of unit cells in each layer, $N_{s,z}$. For each mode, we apply an actuation to deform the structure to the maximum attainable angle, that is, $(\theta_t, \theta_b) = (\pi/2, \pi/2)$ for the compression mode, and $(\theta_t, \theta_b) = (\pi/2, 0)$ for the bending mode. We then obtain the normalized elastic energy for these deformations. The compression mode does not show any

increase in energy for greater $N_{s,x}$, $N_{s,y}$ or $N_{s,z}$, implying that this mode exists independently from the number of unit cells in the structure. By assuming a stiffness for the hinges that is nonzero, the average deformation energy per unit cell remains equal, since along the compression mode, there is no face deformation, only hinge folding. This result implies that the local actuation triggers a global deformation where all angles of the hinges in the structure depend on only one DOF, following the ideal behavior.

In contrast, we see a decrease of the average energy when increasing the number of layers, $N_{s,z}$ (Figure 3F). The applied actuation lies only at the top and bottom layers, so by increasing $N_{s,z}$, we do not increase the actuation, but instead increase the number of unit cells in the array. This increase of unit cells, together with constant actuation, leads to a decrease in the average energy, demonstrating that the deformation is not global, as with the compression mode, but instead takes place primarily at the top and bottom layer.

Furthermore, we calculate the curvature of the material to understand the scaling of the deformation due to the bending mode. The curvature allows us to estimate the general deformation of the structure, which is calculated by fitting the top and bottom faces of the structure to a sphere. We then average the radii of these two spheres (r), and obtain the Gaussian curvature ($K = 1/r^2$) of the structure as a whole. Figure 3G shows this curvature as a function of $N_{s,z}$. We observe that the curvature decreases with $N_{s,z}$ tending to zero for all arrays irrespective of $N_{s,x}$, $N_{s,y}$. This result implies that in the limit of infinitely large arrays (i.e., $N_{s,x}$, $N_{s,y}$ and $N_{s,z}$ tends to infinity), the structure remains flat. Note that in this limit, the top and bottom layers still deform, but do not trigger a global deformation as compared to the compression mode.

From these analyses, we observe that the compression mode is scale-independent and can be studied by only analyzing the bending of the hinges. On the contrary, the bending mode is dependent on off-axis (e.g., shear or twist, deformation of the hinges), and as such, deforms the structure only locally.

2.3. Empirical Characterization of the Compression Mode

Based on the analysis above, we focus on physically characterizing the scale-independent compression mode. To understand the behavior of the metamaterial along the compression mode, failure and cyclic tests were performed on arrays with $N_{s,x} = N_{s,y} = 3$ and varying $N_{s,z}$ from one to three. The results of these experiments are shown in **Figure 4**, where we plot force versus displacement instead of stress versus strain since the maximum number of units cells is small (<30).

For the failure tests, the arrays were placed unconstrained between the two low-friction plates and compressed from the side until failure (i.e., delamination or tearing of hinges), which occurred at the maximum compression shown for each array

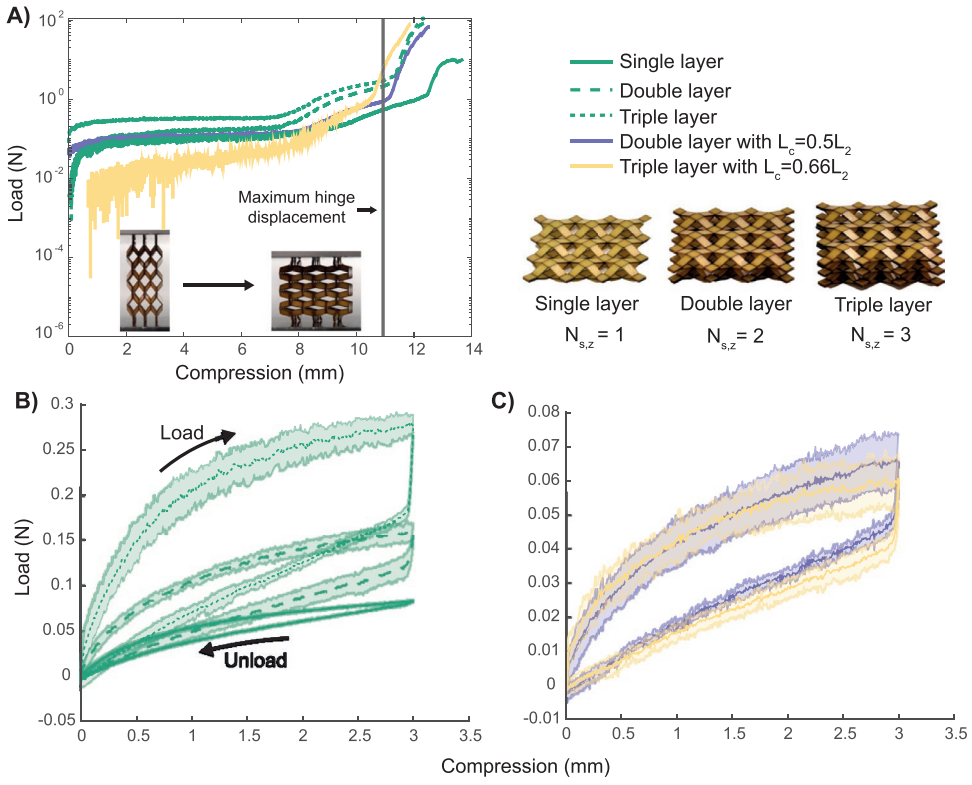

Figure 4. Metamaterial array characterization. A) Failure testing under compression from the side. The array is placed unconstrained between two low-friction compressive plates, and fails due to delamination or tearing of the hinges, which occurs at the maximum compression shown for each array. B) Elastic cyclic testing for single, double, and triple layer Sarrus arrays with no cutouts ($L_c = 0$). C) Elastic cyclic testing for double and triple layer Sarrus arrays with $L_c = 0.5L_2$ and $L_c = 0.66L_2$, respectively. Shaded regions in (B,C) correspond to ± one standard deviation ($n = 4$ cycles).

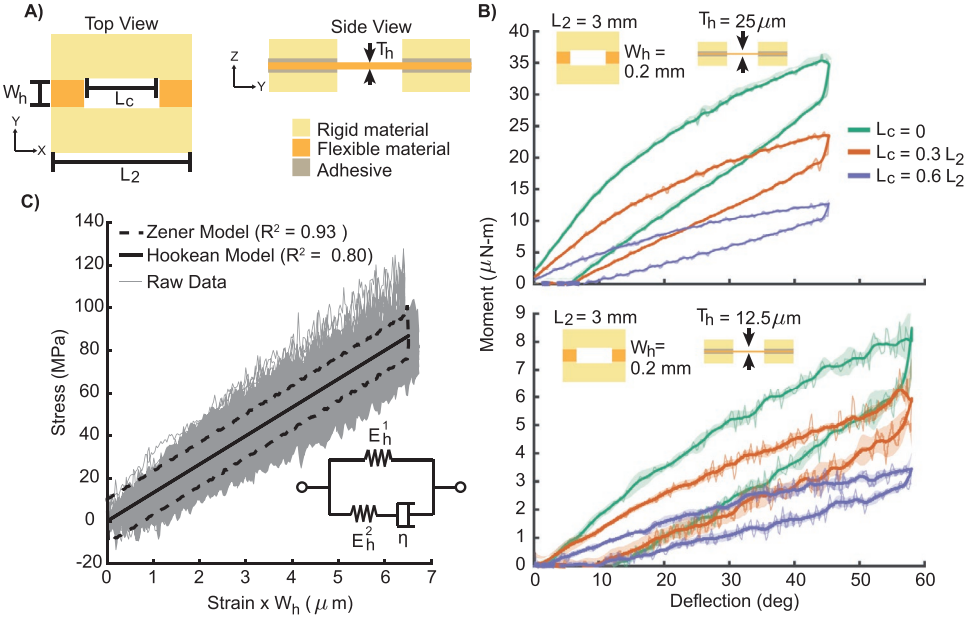

Figure 5. Experimental hinge characterization. A) A schematic of the top and side view of a hinge with the four design parameters labeled. B) The effect of varying cutout width, L_c, on hinge stiffness for 25 µm (top) and 12.5 µm (bottom) thick hinges. The shaded regions represent ± one standard deviation ($n = 5$ trials). See Figure S2, Supporting Information for the effect of varying hinge length, W_h, and hinge width, L_2, on stiffness. C) Hookean and Zener best-fit models plotted alongside normalized stress–strain curves for all tested hinges (24 hinges, five trials each). Note that we plot the product of the strain and W_h on the x-axis to normalize the strain experienced by hinges of different lengths, W_h.

(Figure 4A). We also find three different stiffness regimes: a low-strain region (compression less than 8 mm) where the stiffness (i.e., slope) of all tested arrays remains relatively constant, an intermediate-strain region (compression between 8 and 11 mm) where the stiffness increases moderately, and a high-strain region (compression greater than 11 mm) where the stiffness increases significantly. We propose that this behavior in the low-strain region is determined by on-axis hinge bending, whereas the high-strain region response is determined by collisions between the rigid faces. This hypothesis is supported by the fact that a compression of 11 mm approximately corresponds to the maximum deflection the hinges can experience: $\theta_{max} = \frac{2W_h}{T_f} = 75^\circ$ before the rigid faces collide. The stiffness increase in the intermediate-strain region is likely due to manufacturing imperfections that cause collisions between some faces before θ_{max} is reached, differences in the loading conditions for hinges on the edge of the array, or a combination of the two.

For the cyclic tests, arrays were also placed in the testing device so that they were loaded from the side, moving along the compression mode. The arrays were again placed unconstrained between the two low-friction compressive plates. As shown in Figure 4B, the structure exhibited viscoelastic behavior, namely strain softening, stress relaxation, and hysteresis, which could likely be due to plastic deformation of the hinges. Moreover, the stiffness increased approximately linearly with the number of layers. We also found that, as expected, the effective modulus of the structure was approximately equal for all three arrays (Figure S4B and Note S2, Supporting Information). Note that variations in effective modulus were due to small variations in the initial (i.e., equilibrium), configuration of the array as the modulus was a function of the array's initial configuration.

We also introduced hinge cutouts (see **Figure 5**A for details) as a method for altering the stiffness of the hinges without changing their length, W_h, width, L_2, or thickness, T_h. As shown in Figure 5A, a cutout was a centered rectangular hole of length W_h and width $L_c < L_2$ removed from the hinge to reduce its bending stiffness. Adding cutouts can also be used to reduce the modulus of the array (Figure S4B, Supporting Information). Moreover, we show that it is possible to design a two layer or three layer Sarrus array with the same stiffness as a single-layer array when appropriately sized cutouts are used in the hinge design (Figure 4C). Here, we use $L_c = 0.5L_2$ for the two-layer array and $L_c = 0.66L_2$ for the three-layer array. Consequently, cutouts in the hinges provide a design tool for controlling the modulus of the metamaterial without changing hinge, and therefore, metamaterial geometry.

2.4. Analytical Model of the Hinges

To develop a deeper understanding of the compression mode, we focus on characterizing the hinge bending. We build an empirically-verified analytical description of the hinges that allows us to control the stiffness, k, of the hinge by modifying its geometric parameters. This model is then used to verify the behavior observed along the compression mode. Our hinges have a rectangular geometry defined by four parameters: the hinge width L_2, the cutout width L_c, the hinge length W_h, and the hinge thickness T_h (Figure 5A). In order to behave as a small-length flexural pivot, we impose the constraint that the hinge width is much greater than its length, which is much greater than its thickness, that is $L_2 \gg W_h \gg T_h$.

We tested a total of 24 hinges with different lengths, widths, cutout widths, and thicknesses to understand the effect of varying the geometric parameters described above. Representative results from these tests are shown in Figure 5B, where we plot the measured bending moment versus hinge rotation for hinges with three cutout widths ($L_c = 0, 0.3L_2, 0.6L_2$), each with two thicknesses ($T_h = 25$ and 12.5 μm). The average slope of the curves represents the bending stiffness. As expected, we saw that bending stiffness decreased with increasing cutout width, L_c and increased with increasing hinge thickness, T_h (Figure 5B). The effect of hinge length, W_h, and width, L_2, are shown in Figure S2, Supporting Information, and as expected, we found that bending stiffness decreased with increasing hinge length and increased with increasing hinge width. Again, as expected, the hinge bending stiffness was more sensitive to changes in thickness than in length, width, or cutout width, thus providing guidelines for tuning this stiffness. Finally, we note that these hinges can experience considerable loading cycles before failure. Figure S3, Supporting Information, shows that the behavior of our hinges does not change across 20 loading cycles. Moreover, Malka et al.[54] tested the fatigue behavior of polyimide hinges (Dupont, Kapton) with similar geometries and found that failure occurs between 10^4 to 10^6 cycles.

To analytically understand this behavior, we modeled the hinge response as a cantilevered beam using the Euler–Bernoulli expression, which related the bending moment, M, experienced by the hinge to its rotation, θ, by a constant stiffness k:

$$M = k\theta, \text{ with } k = \frac{E_h L_{eff} T_h^3}{12 W_h} \tag{2}$$

Here E_h is the elastic modulus of the hinge material (polyimide), and $L_{eff} = L_2 - L_c$ is the effective width of the hinge. Combining this with a Hookean model that relies on a linear elastic relationship between the bending stress, σ_b, and strain, ε, at the surface of the hinge material, we obtain the relation[55]

$$\sigma_b = E_h \varepsilon, \text{ with } \sigma_b = \frac{6M}{L_{eff} T_h^2} \text{ and } \varepsilon = \frac{T_h \theta}{2 W_h} \tag{3}$$

However, we experimentally observe that the hinges exhibit viscoelastic behavior, which likely causes the viscoelasticity observed in the structure. This behavior is to be expected, as local strain in the hinges reached up to 5% during testing, beyond the yield strain of 3%.[51] Consequently, we replace the Hookean linear-elastic relationship between bending stress and strain with the viscoelastic Zener or standard linear solid model. The constituent law for this model is given by the following differential equation,

$$\sigma_b + \frac{\eta}{E_h^2} \dot{\sigma}_b = E_h^1 \varepsilon + \frac{\eta (E_h^1 + E_h^2)}{E_h^2} \dot{\varepsilon} \tag{4}$$

Here η, E_h^1, and E_h^2 are defined in the inset of Figure 5C and the dot superscript represents differentiation with respect to time.

We estimate the parameters of the Zener model using a linear regression where ε and σ_b were computed from the raw moment/rotation data using Equation (3). The time derivatives of ε and σ_b are computed by taking the finite difference of ε and σ_b after filtering with an acausal moving average filter. The estimated values of η, E_h^1, and E_h^2 are 80.2 GPa s, 2.71 GPa, and 160.30 GPa, respectively. We also estimate the parameters for the linear-elastic model defined in Equation (2). As expected, E_h is also equal to 2.71 GPa. This value and the equilibrium stiffness of the Zener model, E_h^1, agrees well with the datasheet value for the elastic modulus of the polyimide (2.71 GPa,[51]). However, by comparing both models against the empirical data in Figure 5C, we see that the Zener model (dashed) is able to capture the viscoelastic behavior of the polyimide while the linear elastic model (solid) does not. Consequently, the coefficient of determination R^2 for the Zener model (0.93) was higher than that of the linear-elastic model (0.80). This result demonstrates that the hinge is viscoelastic, entailing the dissipation of energy and plastic deformation. Nevertheless, the Hookean model still captures the basic behavior, and due to its linearity, we use this result to develop a static model of the array along the compression mode.

2.5. Analytical Model of the Compression Mode

In the numerical model, the compression mode is a rigid folding mode where all deformation is localized to the hinges and the faces remain rigid. Consequently, we can use the hinge model developed in the previous section to predict the force required to compress the metamaterial along the compression axis as shown in Figure 4A. The potential energy of the array is

$$V = \sum_{i=1}^{N_f} \frac{1}{2} k_i (\theta_i - \theta_0)^2 \tag{5}$$

where $N_f = 16 N_{s,z} N_{s,x} N_{s,y}$ is the total number of hinges in the array, k_i is the Hookean stiffness of the i-th hinge (Equation (2)), θ_i is the angular deflection of the i-th hinge, and $\theta_0 = 32°$ is the average initial plastic deformation of the hinge. Moreover, $N_{s,x} N_{s,y}$, $N_{s,z}$ are the number of unit cells in x, y, and z-directions, respectively, as defined in Figure 1C. We then differentiate this expression to compute the force required to compress the array as $F_x = -\frac{\partial V}{\partial x}$. Assuming all hinges deflect equally, we can use the geometry of the array to solve for θ_i in terms of the array's displacement along the compression axis x:

$$\theta_i = \cos^{-1}\left(\frac{x}{\sqrt{2} N_{s,x} L_1} - \frac{(N_{s,x} + 1) L_2}{N_{s,x} L_1} \right) \tag{6}$$

where L_1 and L_2 are geometric parameters defined in Figure 1. Further details on the derivation of Equation (6) are provided in Note S2, Supporting Information. We then obtain the following force–displacement relation after substituting Equation (6) into Equation (5) and compute the derivative:

$$F_x = -\sum_{i=1}^{N_f} k_i (\theta_i - \theta_0) \frac{\partial \theta_i}{\partial x} \tag{7}$$

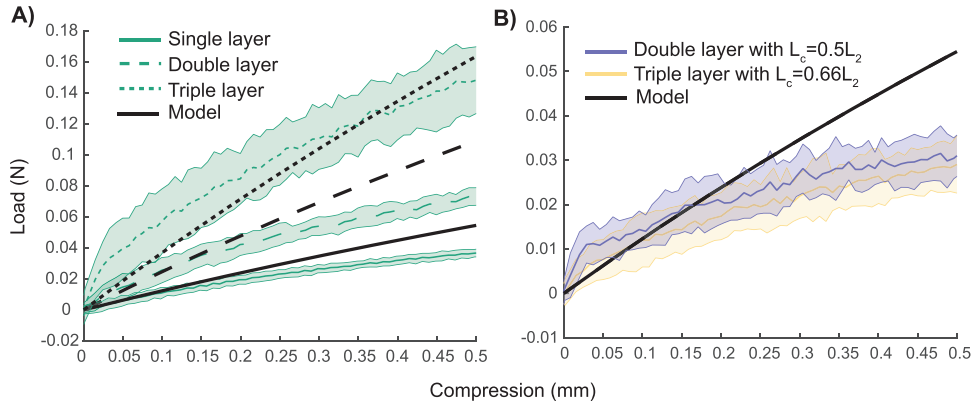

Figure 6. Analytical model of the compression mode. A) Small deformations for elastic cyclic testing for single, double, and triple layer Sarrus arrays with $L_c = 0$. B) Small deformation with elastic cyclic testing for double and triple layer Sarrus arrays with $L_c = 0.5L_2$ and $L_c = 0.66L_2$, respectively. Shaded regions correspond to ± one standard deviation ($n = 4$ cycles), and the model-predicted force Equation (7) is shown in black for both (A,B).

where

$$\frac{\partial\theta_i}{\partial x} = \frac{-1}{\sqrt{2}N_{s,x}L_1}\left(1-u(x)^2\right)^{-\frac{1}{2}}, \text{ and } u(x) = \left(\frac{x}{\sqrt{2}N_{s,x}L_1} - \frac{(N_{s,x}+1)L_2}{N_{s,x}L_1}\right) \tag{8}$$

As seen in **Figure 6**A,B, this description approximately matches the experimental results for small displacements (⩽0.5 mm). The discrepancy between these two curves is likely due to a violation of the assumption of equal hinge deflections, especially near the array boundaries, during the experiments. We also see in Figure S4C, Supporting Information that this model captures the change in modulus caused by introducing cutouts. However, this approximation does not capture strain softening and hysteresis that occurs at large strains. Consequently, this model can be used to approximately calculate the stiffness of these arrays along the compression mode, and as a qualitative design tool for modulating array stiffness (e.g., increasing cutout width to reduce stiffness).

Moreover, we show that this analytical model can also be used to calculate other properties of interest, focusing on volumetric change, which could be a quantity of interest for potential acoustic applications. In supplementary Note S3, Supporting Information, we define and compute volumetric change using both the analytic and numerical models. The results of this analysis are shown in Figure S5, Supporting Information. We find that both models agree, and that while volumetric change has a slight dependence on array size, this dependence disappears as the array size increases.

3. Conclusion

In this paper, we used laminate manufacturing to fabricate a flat-foldable millimeter-scale metamaterial, bridging the gap between macro- and micro-scale geometries. The key advantages of this design and fabrication process are its ability to utilize a wide range of manufacturing materials, as well as enabling the design of complex, that is, ⩾ 1000 hinges, arrays with minimal manual assembly. We demonstrated the utility of this approach by fabricating a metamaterial based on a four-sided Sarrus linkage and then explored the behavior of the resulting array. Contrary to the behavior predicted by the kinematic model, we experimentally found two deformation modes: compression and bending. We then built a numerical model to show that the bending mode depended on off-axis deformation of the hinges and it became a local mode as the metamaterial increases in size. Consequently, we focused on quantitatively characterizing the compression mode, which depends on the bending of the hinges, and its behavior can be controlled through hinge design. To better understand this mode, we built two models of hinge bending that predicted Hookean and viscoelastic modulus as a function of geometry. We found that the Hookean model was a good approximation for small deformations, and could be used to predict the modulus of the metamaterial along the compression mode. Overall, we demonstrated the advantages of using laminate manufacturing for metamaterial fabrication and developed several models to help design linkage arrays and predict their behavior.

While a four-sided Sarrus linkage was chosen due to its simplicity and scalability, our fabrication method allows for more complicated structures that can be described using rigid faces and bendable hinges. For example, alternate unit cells can also be used. **Figure 7** shows a simple extension that uses three-sided and six-sided Sarrus linkages. These alternative

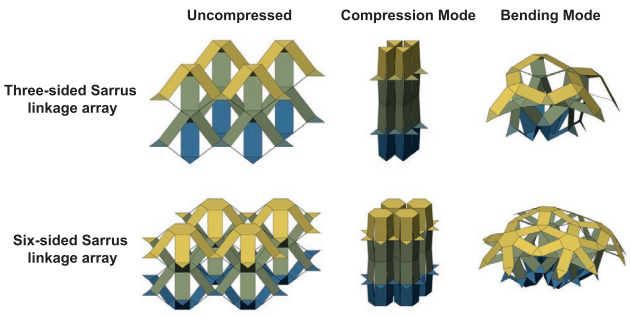

Figure 7. Alternative Sarrus linkage array geometries. Examples of alternative array geometries include using three-sided or six-sided Sarrus linkages. Despite the altered geometry, the structures still display the same bending modes as the four-sided Sarrus linkage array.

geometries still exhibit the same bending modes as the four-sided linkage array, as the base mechanism exhibits the same deformations. While it is also possible to use heterogeneous unit cells in the same array, it is important to carefully analyze how the off-axis deformation of the hinges propagates through the structure.

Moreover, by altering the unit cell size, we can produce metamaterials that bridge the gap between the macro- and micro-scale for a variety of applications. On the one hand, arrays with larger unit cells can be fabricated using subtractive manufacturing methods with a larger workspace (e.g., a carbon dioxide laser, water jet, electrical discharge machining) and with a choice of materials and laminate geometries that satisfy the pseudo-rigid body assumptions.[44] On the other hand, the minimum size of the unit cell is determined by the resolution of the technique used for bullk micromachining. However, there are two other practical limitations. First, the availability of raw materials sets a lower bound on unit cell size. Based on Howell's design guidelines,[44] the hinge width must be ≈100 × its thickness. Additionally, the laminate material must either have a higher modulus or its thickness and length must be ≈10 × the hinge thickness and length, respectively. Second, the fabrication process still requires some manual assembly, which could be automated using the methods described by Sreetharan et al.[39] With the current setup, however, we found that further downscaling of the samples does not seem feasible, but by addressing these two limitations, we could potentially further reduce the size of the unit cell.

Finally, we anticipate that this fabrication method could enable the development of reconfigurable metamaterials with broad applications. The structure's reconfigurability from a flat configuration can be used, for example, in the design of deployable structures for medical applications such as stent grafts.[22] This reconfigurability could also enable programmable, multifunctional electromagnetic responses in multilayer structures, improving previous work on single-layer structures.[47] These applications thus demonstrate the potential versatility of this new class of metamaterials and the ability to actively tune their functionalities.

4. Experimental Section

Fabrication of Sarrus Linkage Arrays: The Sarrus linkage arrays were fabricated using laminate manufacturing processes. For a single array, fabrication occurs in four steps: 1) Stiff, flexible, and adhesive layers were individually cut using a laser micromachining system (Oxford Lasers) according to design cut files. Sheets of 125 µm FR4 (McMaster-Carr), carbon fiber (Q1-112, Tohotenax), and 50 µm stainless steel shim coil (Maudlin Products) were used for stiff layers. Polyimide films (Kapton, DuPont) of thickness 7.5, 12.5, and 25 µm were used for the flexible layers and heat and pressure activated sheet adhesive (Pyralux FR1500, DuPont) was used for the adhesive layer.

2) Stiff and flexible layers were cleaned with isopropyl alcohol. Carbon fiber and stainless steel substrates were also plasma etched (Diener) for enhanced bonding.

3) Layers were laterally aligned for lamination using precision dowel pins and cured together at a temperature of 200° and a pressure of 25 psi for approximately 2.5 h.

4) The resulting laminate was micromachined again to release the array from the surrounding bulk material. To fabricate multilayered arrays, an additional cure cycle and release cut was added to bond arrays to each other.

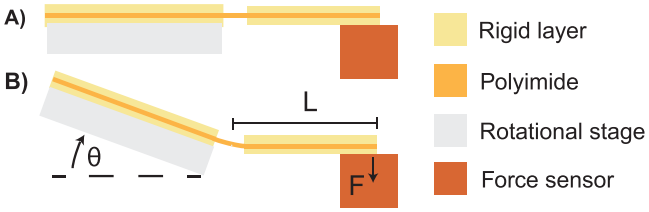

Figure 8. A schematic of the experimental set-up for hinge bending stiffness tests in A) its starting configuration and B) a deformed configuration. The hinge angle, θ, the beam length, L, and the force applied by the beam-tip, F, are recorded. Hinge stiffness is calculated as the ratio between hinge angle and the measured torque, i.e., the product of L and F.

Single Hinge Testing: A total of 24 different hinges in 1D studies were tested for hinges of three different widths (L_2 = 120, 240, and 360 µm), three different lengths (W_h = 1, 2, and 3 mm), three different cutout widths (L_c = 0, 0.33L_2, and 0.66L_2), and two different thicknesses (T_h =12.5 and 25 µm).

The bending stiffness of each hinge was measured five times using a custom test setup (**Figure 8**). The hinge was fastened to a rotational stage (Newport URB100cc) whose center of rotation was visually aligned with the approximate center of rotation of the hinge. Before each trial, a single-axis force sensor (Futkek LSB 200) was raised using a micro-positioning stage until it was just under the hinge (Figure 8A). The rotational stage was then driven using a trapezoidal profile with a ramp velocity of approximately 20° s^{-1} and the vertical force F exerted by the hinge on the force sensor was recorded at ≈75 Hz. Note that slip between the tip of the hinge and the force sensor was minimized by aligning the rotational centers of the hinge and the stage. Finally the force recorded by the sensor was converted into a bending moment experienced by hinge by multiplying by the effecting moment arm L.

Metamaterial Testing: Single, double, and triple layer Sarrus arrays fabricated with 125 µm FR4 and 12.5 µm polyimide were tested using a 2 kN load cell on a universal materials testing device (Instron 5544A, Illinois Tool Works, Norwood, MA). Arrays were cyclically compressed 3 mm at a rate of 5 mm min^{-1} for four cycles to capture the elastic deformation of the arrays, which was approximately equal to bending each hinge at a rate of 1° s^{-1} if all hinges were assumed to bend equally. It should be noted that this approach was different from the single hinge testing rate, and might lead to different amounts of hysteresis. The arrays were also compressed until failure in the xy plane and xz plane and compressed in their flattened state to demonstrate the compressibility of the laminates. Force and displacement measurements were recorded simultaneously.

Supporting Information

Supporting Information is available from the Wiley Online Library or from the author.

Acknowledgements

H.D.M., N.D., and A.I.-R. contributed equally to this work. This work is part of the Dutch Research Council (NWO) and was performed at the research institute AMOLF. It is part of the research program Innovational Research Incentives Scheme Veni from NWO with project number 15868 (NWO). This research was also partially supported by an appointment to the Intelligence Community Postdoctoral Research Fellowship Program at the Massachusetts Institute of Technology, administered by Oak Ridge Institute for Science and Education through an interagency agreement between the U.S. Department of

Energy and the Office of the Director of National Intelligence. Finally, this research was also funded in part by the NASA Space Technology Research Fellowship.

Conflict of Interest

The authors declare no conflict of interest.

Data Availability Statement

The data that support the findings of this study are available from the corresponding author upon reasonable request.

Keywords

flat-foldable, metamaterials, reconfigurable

Received: April 10, 2021
Revised: July 5, 2021
Published online:

[1] Z. G. Nicolaou, A. E. Motter, *Nat. Mater.* **2012**, *11*, 608.
[2] K. K. Dudek, D. Attard, R. Caruana-Gauci, K. W. Wojciechowski, J. N. Grima, *Smart Mater. Struct.* **2016**, *25*, 025009.
[3] Q. Wang, J. A. Jackson, Q. Ge, J. B. Hopkins, C. M. Spadaccini, N. X. Fang, *Phys. Rev. Lett.* **2016**, *117*, 175901.
[4] A. Martin, M. Kadic, R. Schittny, T. Bückmann, M. Wegener, *Phys. Rev. B* **2012**, *86*, 155116.
[5] X. Yu, J. Zhou, H. Liang, Z. Jiang, L. Wu, *Prog. Mater. Sci.* **2018**, *94*, 114.
[6] S. Babaee, J. Shim, J. C. Weaver, E. R. Chen, N. Patel, K. Bertoldi, *Adv. Mater.* **2013**, *25*, 5044.
[7] H. Yasuda, J. Yang, *Phys. Rev. Lett.* **2015**, *114*, 185502.
[8] F. Ding, Y. Cui, X. Ge, Y. Jin, S. He, *Appl. Phys. Lett.* **2012**, *100*, 103506.
[9] J. Tak, J. Choi, *IEEE Antennas Wireless Propagation Lett.* **2016**, *16*, 784.
[10] S. A. Cummer, J. Christensen, A. Alù, *Nat. Rev. Mater.* **2016**, *1*, 16001.
[11] J. Mei, G. Ma, M. Yang, Z. Yang, W. Wen, P. Sheng, *Nat. Commun.* **2012**, *3*, 756.
[12] V. M. Shalaev, *Nat. Photonics* **2007**, *1*, 41.
[13] J. Valentine, S. Zhang, T. Zentgraf, E. Ulin-Avila, D. A. Genov, G. Bartal, X. Zhang, *Nature* **2008**, *455*, 376.
[14] K. Miura, *Inst. Space Astronaut. Sci. Rep.* **1985**, *618*, 1.
[15] Z. Lin, L. S. Novelino, H. Wei, N. A. Alderete, G. H. Paulino, H. D. Espinosa, S. Krishnaswamy, *Small* **2020**, *16*, 2002229.
[16] Z. Zhao, X. Kuang, J. Wu, Q. Zhang, G. H. Paulino, H. J. Qi, D. Fang, *Soft Matter* **2018**, *14*, 8051.
[17] J. T. Overvelde, T. A. De Jong, Y. Shevchenko, S. A. Becerra, G. M. Whitesides, J. C. Weaver, C. Hoberman, K. Bertoldi, *Nature Commun.* **2016**, *7*, 10929.
[18] K. Liu, T. Tachi, G. H. Paulino, *Nat. Commun.* **2019**, *10*, 4238.
[19] Y. Yang, Z. You, *J. Mech. Rob.* **2018**, *10*, 2.
[20] Y. Yang, Z. You, *arXiv:2012.09567*, **2020**.
[21] Y. Chen, R. Peng, Z. You, *Science* **2015**, *349*, 396.
[22] K. Kuribayashi, K. Tsuchiya, Z. You, D. Tomus, M. Umemoto, T. Ito, M. Sasaki, *Mater. Sci. Eng., A* **2006**, *419*, 131.
[23] K. C. Cheung, T. Tachi, S. Calisch, K. Miura, *Smart Mater. Struct.* **2014**, *23*, 094012.
[24] B. Haghpanah, H. Ebrahimi, D. Mousanezhad, J. Hopkins, A. Vaziri, *Adv. Eng. Mater.* **2016**, *18*, 643.
[25] B. Florijn, C. Coulais, M. van Hecke, *Phys. Rev. Lett.* **2014**, *113*, 175503.
[26] J. Shim, S. Shan, A. Košmrlj, S. H. Kang, E. R. Chen, J. C. Weaver, K. Bertoldi, *Soft Matter* **2013**, *9*, 8198.
[27] J. T. Overvelde, J. C. Weaver, C. Hoberman, K. Bertoldi, *Nature* **2017**, *541*, 347.
[28] B. Haghpanah, L. Salari-Sharif, P. Pourrajab, J. Hopkins, L. Valdevit, *Adv. Mater.* **2016**, *28*, 7915.
[29] E. Hawkes, B. An, N. M. Benbernou, H. Tanaka, S. Kim, E. Demaine, D. Rus, R. J. Wood, *Proc. Natl. Acad. Sci. U. S. A.* **2010**, *107*, 12441.
[30] N. An, A. G. Domel, J. Zhou, A. Rafsanjani, K. Bertoldi, *Adv. Funct. Mater.* **2020**, *30*, 1906711.
[31] L. R. Meza, S. Das, J. R. Greer, *Science* **2014**, *345*, 1322.
[32] J. Bauer, S. Hengsbach, I. Tesari, R. Schwaiger, O. Kraft, *Proc. Natl. Acad. Sci. U. S. A.* **2014**, *111*, 2453.
[33] T. Bückmann, N. Stenger, M. Kadic, J. Kaschke, A. Frölich, T. Kennerknecht, C. Eberl, M. Thiel, M. Wegener, *Adv. Mater.* **2012**, *24*, 2710.
[34] J. Bauer, A. Schroer, R. Schwaiger, I. Tesari, C. Lange, L. Valdevit, O. Kraft, *Extreme Mech. Lett.* **2015**, *3*, 105.
[35] T. A. Schaedler, A. J. Jacobsen, A. Torrents, A. E. Sorensen, J. Lian, J. R. Greer, L. Valdevit, W. B. Carter, *Science* **2011**, *334*, 962.
[36] X. Zheng, H. Lee, T. H. Weisgraber, M. Shusteff, J. DeOtte, E. B. Duoss, J. D. Kuntz, M. M. Biener, Q. Ge, J. A. Jackson, S. O. Kucheyev, N. X. Fang, C. M. Spadaccini, *Science* **2014**, *344*, 1373.
[37] S. Babaee, S. Pajovic, A. Rafsanjani, Y. Shi, K. Bertoldi, G. Traverso, *Nat. Biomed. Eng.* **2020**.
[38] A. Ion, J. Frohnhofen, L. Wall, R. Kovacs, M. Alistar, J. Lindsay, P. Lopes, H.-T. Chen, P. Baudisch, in *Proc .of the 29th Annual Symp. on User Interface Software and Technology*, Association for Computing Machinery, New York, NY, USA **2016** pp. 529–539.
[39] P. S. Sreetharan, J. P. Whitney, M. D. Strauss, R. J. Wood, *J. Micromech. Microeng.* **2012**, *22*, 055027.
[40] R. Wood, S. Avadhanula, R. Sahai, E. Steltz, R. Fearing, *J. Mech. Design* **2008**, *130*, 052304.
[41] A. M. Hoover, R. S. Fearing, in *2008 IEEE Int. Conf. on Robotics and Automation*, IEEE, Piscataway, NJ, **2008**, pp. 886–892.
[42] C. D. Onal, R. J. Wood, D. Rus, in *2011 IEEE Int. Conf. on Robotics and Automation (ICRA)*, IEEE, Piscataway, NJ, **2011**, pp. 4608–4613.
[43] J. P. Whitney, P. S. Sreetharan, K. Y. Ma, R. J. Wood, *J. Micromech. Microeng.* **2011**, *21*, 115021.
[44] L. L. Howell, *Compliant Mechanisms*, John Wiley & Sons, Hoboken, NJ **2001**.
[45] H. McClintock, F. Z. Temel, N. Doshi, J. -s. Koh, R. J. Wood, *Sci. Rob.* **2018**, *3*, eaar3018.
[46] Z. Wang, L. Jing, K. Yao, Y. Yang, B. Zheng, C. M. Soukoulis, H. Chen, Y. Liu, *Adv. Mater.* **2017**, *29*, 1700412.
[47] D. H. Le, Y. Xu, M. M. Tentzeris, S. Lim, *Extreme Mech. Lett.* **2020**, *36*, 100670.
[48] S. Babaee, J. T. Overvelde, E. R. Chen, V. Tournat, K. Bertoldi, *Sci. Adv.* **2016**, *2*, e1601019.
[49] D. Melancon, B. Gorissen, C. J. García-Mora, C. Hoberman, K. Bertoldi, *Nature* **2021**, *592*, 545.
[50] Dupont, *Pyralux FR 1500 Acrylic Sheet Adhesive* **2011**.
[51] Dupont, *Kapton R HN Polyimide Film* **2011**.
[52] M. F. Ashby, D. Cebon, *J. Phys. IV* **1993**, *3*, C7.
[53] A. Iniguez-Rabago, Y. Li, J. T. Overvelde, *Nat. Commun.* **2019**, *10*, 5577.
[54] R. Malka, A. L. Desbiens, Y. Chen, R. J. Wood, in *IEEE/RSJ Int. Conf. on Intelligent Robots and Systems*, IEEE, Piscataway, NJ **2014**, p. 2879.
[55] M. Goldfarb, J. E. Speich, *J. Mech. Design* **1999**, *121*, 424.